



# A HOT FLUX ROPE OBSERVED BY *SDO*/AIA

V. APARNA AND DURGESH TRIPATHI

Inter-University Centre for Astronomy & Astrophysics, Post Bag—4, Ganeshkhind, Pune 411007, India; [aparnav@iucaa.in](mailto:aparnav@iucaa.in)

Received 2015 September 23; accepted 2016 January 7; published 2016 February 29

## ABSTRACT

A filament eruption was observed on 2010 October 31 in the images recorded by the Atmospheric Imaging Assembly (AIA) on board the *Solar Dynamic Observatory* (*SDO*) in its Extreme Ultra-Violet (EUV) channels. The filament showed a slow-rise phase followed by a fast rise and was classified to be an asymmetric eruption. In addition, multiple localized brightenings which were spatially and temporally associated with the slow-rise phase were identified, leading us to believe that the tether-cutting mechanism initiated the eruption. An associated flux rope was detected in high-temperature channels of AIA, namely 94 and 131 Å, corresponding to 7 and 11 MK plasma respectively. In addition, these channels are also sensitive to cooler plasma corresponding to 1–2 MK. In this study, we have applied the algorithm devised by Warren et al. to remove cooler emission from the 94 Å channel to deduce only the high-temperature structure of the flux rope and to study its temporal evolution. We found that the flux rope was very clearly seen in the clean 94 Å channel image corresponding to Fe XVIII emission, which corresponds to a plasma at a temperature of 7 MK. This temperature matched well with that obtained using Differential Emission Measure analysis. This study provides important constraints in the modeling of the thermodynamic structure of the flux ropes in coronal mass ejections.

**Key words:** solar–terrestrial relations – Sun: corona – Sun: coronal mass ejections (CMEs) – Sun: filaments, prominences – Sun: magnetic fields – Sun: UV radiation

**Supporting material:** animations

## 1. INTRODUCTION

Flux ropes are considered to be an integral part of coronal mass ejections (CMEs) in almost all of the existing theories attempting to explain the initiation and evolution of CMEs, though at different epochs during the CME evolution. Currently, there is great controversy surrounding the subject, regarding when and how the flux ropes form. An account of the prediction of epochs of formation of flux ropes in various models is summarized in Tripathi et al. (2009a). A complete understanding of the nature of flux ropes and their evolutions will first lead us to differentiate the various theoretical models currently present and will also have broad implications on the understanding of the physics of CME initiation. The latter is one of the most important questions in the field of solar physics, given its importance and implications on space weather and geospace climate.

Flux-rope-like structures have commonly been observed in coronagraphic observations of CMEs recorded using the Large Angle and Spectrometric Coronagraph (Brueckner et al. 1995; C2&C3) on board the *Solar and Heliospheric Observatory* and Cor-1&2 (Howard et al. 2008) on board *Solar Terrestrial Relations Observatory* spacecraft (Cecconi et al. 2008). However, these observations have only confirmed the eventual presence of flux ropes in CMEs without shedding substantial light on their origin. Therefore, low coronal observations are required. In off limb observations, flux ropes have been identified as large-scale cavities with low density and high temperatures (Gibson & Fan 2006; Gibson et al. 2010; Kucera et al. 2012) and show helical motion of plasma (see e.g., Schmit et al. 2009). These cavities are often related to the large-scale polar crown filaments, where the filament material is located at the bottom of the flux rope and finally appears as a three part structure CME in coronagraphic images (Cremades & Bothmer 2004).

Observations of flux ropes on disks have been difficult due to strong line-of-sight effects. Sigmoids are considered to be one of the best proxies for flux ropes on the solar disk (Gibson et al. 2006; Tripathi et al. 2009a, 2009b). Studying the formation and evolution of sigmoids has given strong evidence toward the pre-existence of flux rope structures (Tripathi et al. 2009b). Tripathi et al. (2009a) compared the observables predicted by a pre-existing flux rope model with observations for six well-observed events, and concluded that these observations could be explained well with the model that has a pre-existing flux rope. However, the direct observation of a flux rope from its birth was not possible until the launch of the *Solar Dynamics Observatory* (*SDO*) in 2010.

Almost all of the models proposed for the formation of a flux rope involve magnetic reconnection, which will lead to emission from hot plasmas. Since all of the Extreme Ultra-Violet (EUV) channels in which the Atmospheric Imaging Assembly (AIA, Lemen et al. 2012) observes are sensitive to plasmas at different temperatures. These observations could be used as a thermometer for coronal plasmas. However, it is nontrivial to interpret the AIA observations directly as temperature diagnostics because AIA channels often have contributions from multiple emission lines sensitive to different temperature plasmas (O’Dwyer et al. 2010). Using the AIA observations of a flaring active region, Reeves & Golub (2011) have constrained the temperature of flux ropes to between 5 and 18 MK, suggesting that the flux ropes could reach flare-like temperatures. In this observation, the flux rope was only observed in 94 and 131 Å channels, which are primarily sensitive to 7 and 11 MK and was not present either in 193 Å or in 171 Å. Nindos et al. (2015) made a survey to establish whether flux ropes commonly exist in CME eruptions in AIA data taken using 131, 171, and 304 Å channels. About 32% of their eruptive events, out of 141, showed features of flux-rope-like structure in 131 Å and none in the rest of the wavelengths,

again suggesting high temperatures of flux ropes. Similarly, Zhang et al. (2015) conducted a large survey that included on-disk as well as limb observations of 1354 “flux-rope proxies.” For about 50% of their events, flux-rope proxies were also seen in 171 and 304 Å. The authors attribute the structures seen in the cooler channels to secondary flux ropes that form due to the reconnection of the coronal arcade and the lifting of cool material higher into the atmosphere during the process (Mackay et al. 2010).

In addition to directly associating a temperature to the structures seen in different AIA channels, which could at times be nontrivial and might be misleading due to contributions from multiple emission lines sensitive to different temperature plasmas, Differential Emission Measure (DEM) inversion methods have also been adopted (see, e.g., Reeves & Golub 2011; Cheng et al. 2012; Patsourakos et al. 2013; Tripathi et al. 2013). A DEM analysis of various regions of the CME structures performed by Cheng et al. (2012) shows a temperature  $>8$  MK for the flux ropes. Tripathi et al. (2013) analyzed a partially erupting prominence using the DEM technique and speculated the presence of a flux rope in the temperature range from 5 to 10 MK. The temperature map of a failed eruption observed by Patsourakos et al. (2013) showed the flux rope structure measuring up to 10 MK. Although, all of these above mentioned studies provide a range of temperature of the flux ropes at a given instance of time, they do not provide the details of the evolution of high-temperature plasma. This is most likely due to the fact that the pixel-wise DEM inversion for narrow band images is a cumbersome and involved process and computationally intensive. Therefore, it may become impractical to perform such a study.

The main aim of this paper is to study the initiation and thermodynamic evolution of the filament eruption and associated flux rope that was observed on 2010 October 31. To this end, we study the kinematics of an erupting filament and associated flux rope and determine the temperature of the flux rope. In addition, we also study how the hot plasma in the flux rope evolves with time during eruption. We have used a novel technique recommended by Warren et al. (2012) to remove the cool temperature component from the 94 Å channel observed by the AIA. The use of this method provides a unique opportunity to study the evolution of true high-temperature plasma in the flux rope, which has not been possible so far due to the reasons mentioned above. The remainder of the paper is structured as follows. In Section 2, we present the observations and data analysis. We discuss the temperature structure of the associated flux rope in Section 3. Finally, we summarize the results and conclude in Section 4.

## 2. OBSERVATIONS AND ANALYSIS

A filament eruption from a small active region situated in the northern hemisphere of the Sun on 2010 October 31 was recorded by AIA on board *SDO*. AIA observes the Sun in nine channels, namely 94, 131, 171, 193, 211, 304, 335, 1600, and 1700 Å. The first six channels primarily correspond to the different ionization states of iron. Although, only one wavelength is assigned to each channel, multiple spectral lines contribute to the whole emission in the respective solar images. For example, the 94 Å channel has contributions from the Fe XVIII at 93.93 Å line as well as emission due to Fe X forming at a wavelength of 94.01 Å among other weaker lines. Similar is the case for 131 Å as well as the other channels. For more

information, see O’Dwyer et al. (2010), Del Zanna et al. (2011), Lemen et al. (2012), and Boerner et al. (2012) regarding the AIA instrument and the responses of various channels due to different kinds of plasma.

Since the aim of this work is to study the high-temperature structure of flux ropes, we concentrate on the high-temperature channels of AIA, namely the 94 and 131 Å channels. However, as mentioned earlier, these channels are contaminated with warm emissions coming from the corona, corresponding to various loop structures as well as the diffuse emission that peaks around  $\log T = 6.25$ , which is characteristic of the 193 Å channel. By doing a comparison of various observations recorded by 94 Å along with that of 171 and 193 Å channels, Warren et al. (2012) devised a scheme to obtain the emission due to the pure Fe XVIII line, which corresponds to plasma at a temperature of  $\sim 7$  MK.

Therefore, in this study, we have applied the algorithm developed by Warren et al. (2012) to the filament eruption in order to separate the hot components from the cooler ones. In order to estimate the higher temperature component in the 94 Å, Warren et al. obtained the following scheme:

$$I_{94\text{warm}} = 0.39 \sum_{i=0}^3 a_i \left[ \frac{f I_{171} + (1-f) I_{193}}{116.54} \right]^i. \quad (1)$$

The value of  $f$  is taken as 0.31 such that the estimated intensities correlate well with the observed intensities. The coefficients of the polynomial fit are  $-7.31 \times 10^{-2}$ ,  $9.75 \times 10^{-1}$ ,  $9.9 \times 10^{-2}$ , and  $-2.84 \times 10^{-3}$ . The constants are the scaling factors derived from the median intensities. For more details, see Warren et al. (2012). We have also compared our results to that obtained using the Del Zanna (2013) algorithm for the removal of the lower temperature contribution in the 94 Å channel.

### 2.1. Overview of the Eruption

The filament eruption occurs between 07:11 and 07:35 UT and is observed in all of the EUV channels of AIA. Figure 1 displays the region of interest on the solar disk in 304 Å (left panel) and a blow-up of the boxed region in the right panel in 193 Å. The filament eruption begins at 07:11 UT from the coordinates [522, 528] arcsec, where intense brightening is seen in 94 and 131 Å at 07:11 UT. Figure 2 displays the sequence of images showing the evolution of the eruption. Running difference images are obtained using 193 Å by subtracting an average of three images prior to every image (Sheeley et al. 2014). Different structures are labelled by arrows in different panels shown in Figure 2.

In order to study the kinematics of the erupting filament, we have created time slice diagrams (TSD) using 193 Å images using three artificial slits across the erupting filament. The left panel in Figure 3 displays the three slits plotted over the AIA image. The right panel shows the TSD obtained for the three slits as labelled. Note that the TSD are obtained using the running-difference images. The eruption is slow in the beginning for about four minutes and shows accelerating features afterward. The slow-rise phase of the eruption lasts until about 07:15 UT and the fast rise occurs between 07:15 and 07:27 UT after which the filament material falls back to the surface toward the southwestern leg and is seen until 07:42 UT. The TSD for slit-1 could be fitted with a second order polynomial and we obtain an acceleration of  $35.59 \text{ km s}^{-2}$ . TSD for slit-2 could be best fitted with an exponential curve

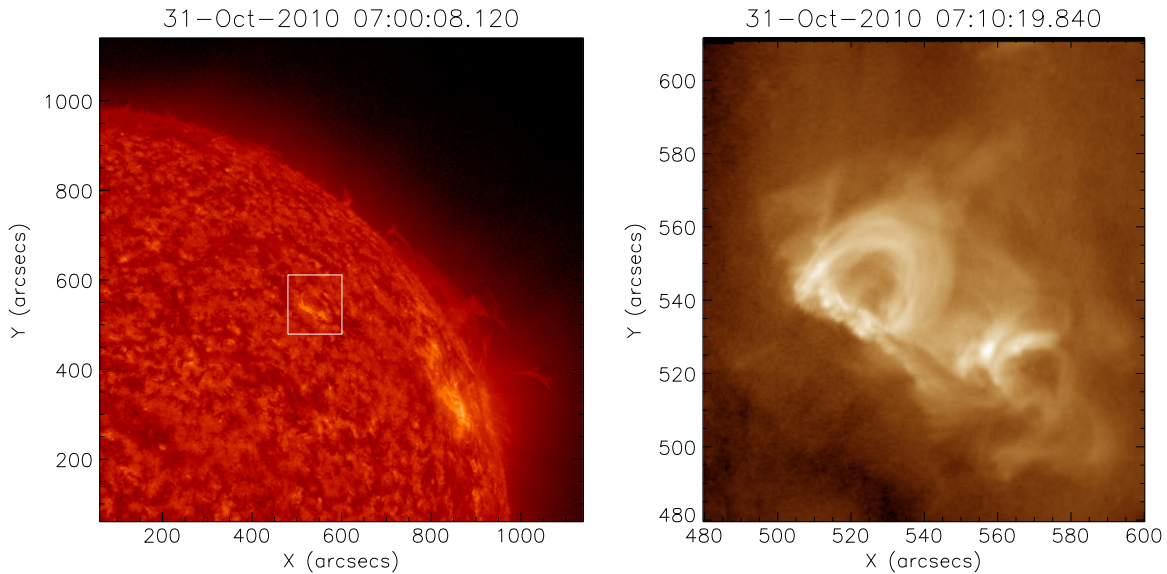


**Figure 1.** Northwestern hemisphere of the Sun on 2010 October 31 (left) shows the region of interest marked by a white bounding box. The region of interest is shown in 193 Å to the right of it.

(curve 1) and a second order polynomial (curve 2, acceleration =  $23.95 \text{ km s}^{-2}$ ). The slow rise in the early phase of the eruption followed by an accelerated phase is apparent. The falling of the material along the southwestern footpoint in the later phase of the eruption is apparent in the bottom panel of Figure 3. The TSDs show that the eruption is asymmetric, which starts from the northeastern footpoint and propagates toward the southwest, as was first described by Tripathi et al. (2006).

In the cooler AIA channels (304, 171, and 193 Å), the filament is seen as a dark absorption feature during the initial rise phase (Figures 2(a) and (b)). The western end of the filament is curved like a “J” and the eastern end is rooted near the brightening region from where the eruption begins. The overlying arcade structure (Martin 1998) engulfing the filament has one foot near the “J” end of the filament and the other foot in front of the eastern end of the “171 loops” (see Figures 2(a) and (b)). The arcade (marked in panel (i) of Figure 2) is pushed higher as the filament erupts. This is seen from 07:17:36 UT until the end of the observations. It expands up to a height of 620'' in the images. The structure is very diffuse at this height and is best seen in 193 Å (Figures 3(g), (h) and (i)). As the filament eruption is in progress, several threads that form the filament get cut. This cutting resembles the tether-cutting as described in Moore et al. (2001), Chifor et al. (2006, 2007), and Liu et al. (2013). These tether-cutting events occur between 07:15:00–07:15:12, 07:17:00–07:17:12, 07:17:48–07:18:00, 07:18:07–07:18:21, and 07:20:36–07:21:24 UT. An example is shown in Figures 2(d) and (e). The filament material does not get ejected, but falls to the surface, some of the threads get tethered from the large arcade structure causing the arcade to rise higher (seen between 07:29:48 and 07:31:48 UT). Blob shaped brightening, localized in space and time, are seen at the locations where the threads are cut in all of these instances of tether cutting.

In the hotter channels of AIA, such as 94 and 131 Å, bright emission is seen prior to the beginning of the filament eruption and continues to brighten along the filament length thereafter. The untwisting of the filament as it rises, the expansion of the

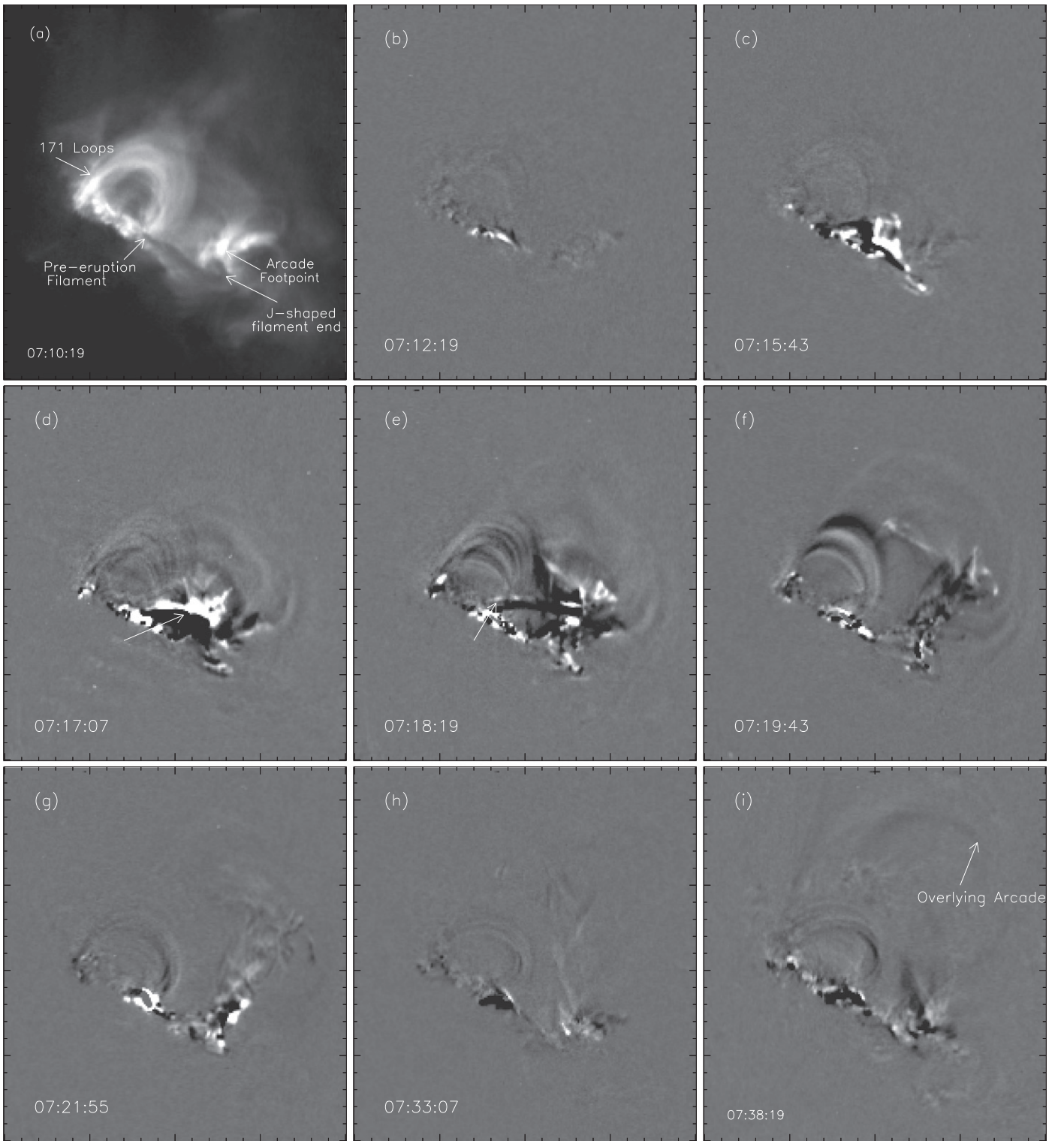
overlying arcade, and the footpoint of the arcade are seen well in 171 and 335 Å. The arcade, its foot, and the loops behind the filament region (marked 171 loops in Figure 2(a)) are visible in the cooler channels except in 304 Å.

Figure 4 shows selected frames in 131, 171, and 94 Å. In 94 and 131 Å, as the filament eruption is under progress, two new strands intertwined with the filament start to rise at 07:15:38 UT. Part of the left-most strand is connected behind the west end of the “171 loops” and part of it along the filament structure (Figures 4(a) and (e)). This is apparent as the two strands continue to rise as a single structure. These strands possibly make the structure of the features seen in the 94 Å images shown in the bottom row in Figure 4. This structure itself is not visible in any of the cooler channels. However, intermittent brightening is seen near the feet of the two strands at around 07:16:12 UT in 171 and 304 Å. The intertwined nature of the flux-rope-like structure is evident between 07:18:09 and 07:18:21 UT in 131 Å when a thin thread connected near the root of the left-most strand is cut from the twisted region in the central part. In 94 and 131 Å, the flux-rope is visible as a diffuse structure (Figures 4(b), (j), (k), and (l)) that rises along with the overlying arcade structure until the end of the observations. The overlying arcade is not seen in 131 Å and is diffuse in 94 Å. As the eruption progresses and the twisted filament structure rises higher, the overlying arcade, visible as a diffuse structure in 171 and 193 Å rises higher owing to the pressure created by the flux rope and the filament. AIA 131 Å records emission due to Fe VIII and Fe XXIII transitions corresponding to  $\sim 0.4$  MK and 14 MK, respectively (O'Dwyer et al. 2010). Because the overlying arcade structure is seen in 94, 171, 193, and 335 and not in 131 Å, the ions in the arcade are expected to measure between 0.6 MK and 2.5 MK.

### 3. TEMPERATURE STRUCTURE OF THE FLUX ROPE

The precise measurement of temperature of the observed flux rope is difficult due to the contamination of the images recorded by AIA as pointed out in Section 2. Therefore, it is important to estimate, if possible, the amount of the cooler





**Figure 2.** Sequence of running-difference images using 193 Å, showing the evolution of the erupting filament, including the untwisting motion. The arrows in figures d and e point to the location of the cutting of the filament threads.

(An animation of this figure is available.)

emission in the hot AIA channels before anything is said about the presence of the hotter component. In order to remove the contribution due to cooler plasma from the 94 Å and to obtain the contribution due to the Fe xviii line, we can use the

algorithms provided by Warren et al. (2012) or Del Zanna (2013). However, this will not be sufficient because the Fe xviii line has a rather broad contribution function and it can form anywhere between 3 and 12 MK with a peak formation

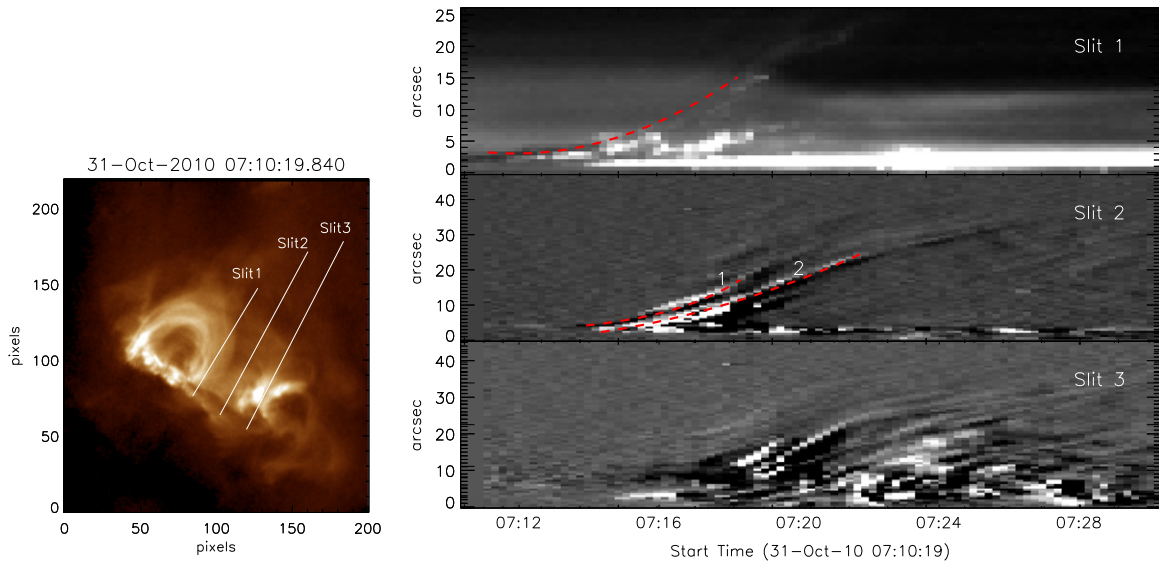


**Figure 3.** Time distance plots of the erupting filament foot for the selected slit positions (left) are shown on the right. The slits track the asymmetric eruption of the filament. The dashed red lines on the time distance plots represent the fitting.

temperature at 7 MK. Therefore, a DEM inversion shall also be necessary to pin-point the temperature of the flux rope.

We apply the algorithm provided by Warren et al. (2012) for our observations of the erupting filament in the 94 Å channel in order to detect the high-temperature structure, if any, of the erupting filament. The eruption begins at 07:11 UT and ends around 07:35 UT. AIA 171 and 193 Å channels provide an estimate of the fluxes whose ratios are used to eliminate the emission due to lower temperatures from the 94 Å channel. This is done on a pixel by pixel basis. All images of the AIA used for this study were processed using standard SolarSoftware (ssw) procedures for AIA and de-rotated to the same time so as to align them perfectly. Several images were blinked to observe the accuracy of alignment of the features. These steps are essential in order to reduce the errors during the pixel to pixel subtraction process of the algorithm. The images are  $201 \times 220$  pixels squared, which corresponds to the region of interest shown by the white-box in the left panel in Figure 1.

Figure 5 displays a sequence of images taken using the 94 Å channel after the subtraction of the emission from cooler plasma. As can be seen, there are no pure Fe XVIII plasma in panel (a) prior to the beginning of the eruption. Figures 5 (b) and (c) show small bright loops that form before the eruption begins. When observed in the Fe XVIII animation, the rise phase of the filament occurs at 07:14:14 in Fe XVIII images whereas without any subtraction, it appears to begin at 07:11:14 UT in the AIA images. This is speculated to be due to the bright emission in the reconnection region leading us to believe that the filament rise starts at an earlier time. At 07:15:26, the strands adjacent to the eastern foot of the rising filament brighten, followed by the emergence of another thread at 07:15:38 UT from the far east end (Figure 5(d)). The two threads continue to rise until 07:17:14 UT after which they expand as a single structure seen as the large loop in panel (e). However, they are only partly connected to each other, some threads have ends behind the “171 loops.” The fact that they are separate loops is evident because there is minimal emission in the region between the two from 07:18:50 and 07:19:50 (see panel (g)) after which some of the threads from the two loops reconnect causing an increase in the emission and a continuous

structure (panel (i)). As the filament rises, the threads get tether-cut (panel (f)) after which the filament structures seen in cooler AIA channels are not seen in Fe XVIII images. This implies that the filament threads have cooled to a lower temperature and thus are not visible in the Fe XVIII.

We believe that the expanding loop structure in the Fe XVIII images is the associated flux rope that is initially twisted at the location where the small loops are seen in the Fe XVIII images. The small loops form due to tether-cutting reconnection and the filament threads are cut during the reconnection due to which it erupts followed by the expansion of the flux rope. The image sequence in Figure 5 reveals the hot nature of the flux rope as the cooler component from the 94 Å channel has been removed. For a few 94 Å images during the course of the eruption, we compared the results obtained using the Warren et al. algorithm with those obtained using Del Zanna’s (2013) algorithm and found that the results were generally consistent with each other.

In order to compare the temperature range of the flux rope using the DEM technique, we compute the DEM of various regions of the flux rope (shown on the right in the top panel in Figure 6). For this purpose, we have adopted the IDL routine provided in SolarSoft *xrt\_dem\_iterative2.pro* (Weber et al. 2004) that computes column DEM. Pre-eruption DEM of the same region (shown on the left in the top panel of Figure 6) is also computed in order to remove the emissions due to the background and foreground. For this computation, we have used Chianti v8 (Dere et al. 1997; Del Zanna et al. 2015) with abundances from Grevesse & Sauval (1998). The EM obtained from the calculated DEM for the three regions, the background and the subtracted EM are shown in the bottom panel in Figure 6. As can be seen, the background EM (i.e., EM computed before the start of the eruption) peaks at  $\log T = 6.5$ , the total EM (i.e., at the time when the flux rope was clearly visible in Fe XVIII images) peaks at around  $\log T = 6.8$ . We note that the low temperature peak is very closely matched with the peak for the background region, suggesting that the cooler temperature peak in the EM curve of the flux rope is most likely due to the omnipresent background emission (Subramanian et al. 2014) and may not have anything



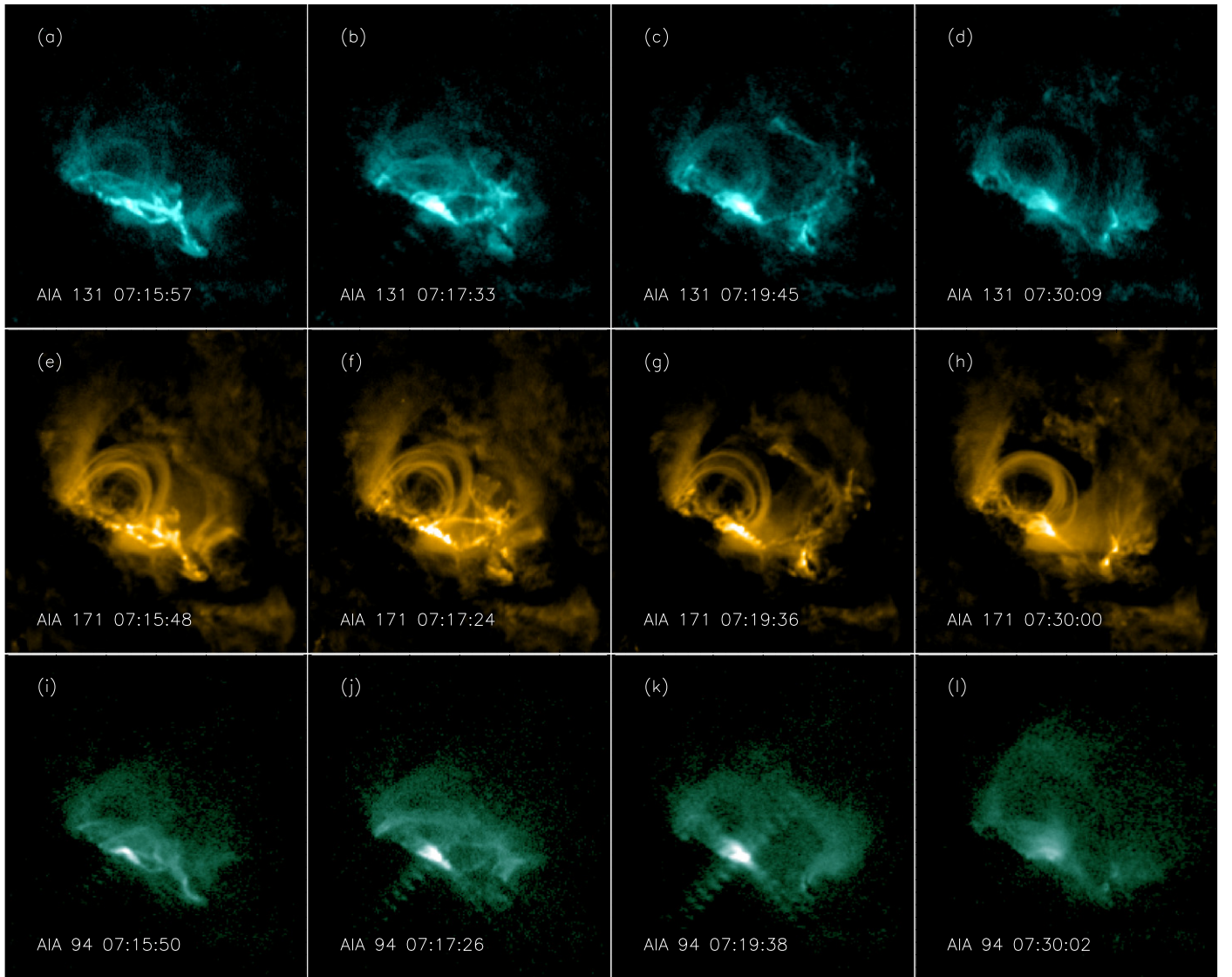


**Figure 4.** AIA 131, 171, and 94 Å images at different times during the filament eruption are shown in the first, second, and third rows, respectively. The flux rope structure is visible in 131 and 94 Å initially (figures (a), (b), (i), and (j)) and can be seen only in 94 Å as the eruption progresses higher (as seen in (k) and (l)).

to do with the erupting flux rope structure. The second peak of the Background EM shown using the smooth line-style is attributed to the heated background as seen in the 94 Å image on the left in Figure 6. The red curve is the difference of the two EM curves, peaking at  $\log T = 7.0$ , providing a range of temperature between  $\log T = 6.7$  and  $\log T = 7.2$ , which roughly coincides with the contribution function of Fe XVIII line formed at 93.9 Å.

#### 4. SUMMARY

An erupting filament observed by *SDO/AIA* on 2010 October 31, between 07:11 and 07:35 UT in all of the EUV channels is studied. We have focussed on the kinematics of the eruption using six EUV channels, identified a flux rope associated with the filament, and obtained its temperature. The main findings of the study are as described below.

1. The filament shows a slow rise followed by a fast-rise phase. Local brightening at the location from where the eruption initially begins is seen following which the

slow-rise phase begins. The eruption is asymmetric and failed. Toward the end of the eruption, the filament material drains toward the solar surface along twisted field lines of one leg of the filament.

2. At the location of the brightening from where the filament eruption occurs, loops are seen when the pixel saturation levels drop toward the end of the eruption. We believe that the tether-cutting-type reconnection mechanism is causing the filament eruption and the formation of the loops.
3. The flux rope associated with the filament starts to rise about two minutes after the filament eruptions begin. It is seen only in the hot channels—94 and 131 Å ( $\sim 11$  MK) images of AIA. The twisted structure of the flux rope is also identified.
4. Since the AIA channels have contributions from other cooler lines and a definitive temperature measure has not been established on flux ropes, we use an algorithm devised by Warren et al. (2012) to remove the cooler emission component. This is used to study the thermal

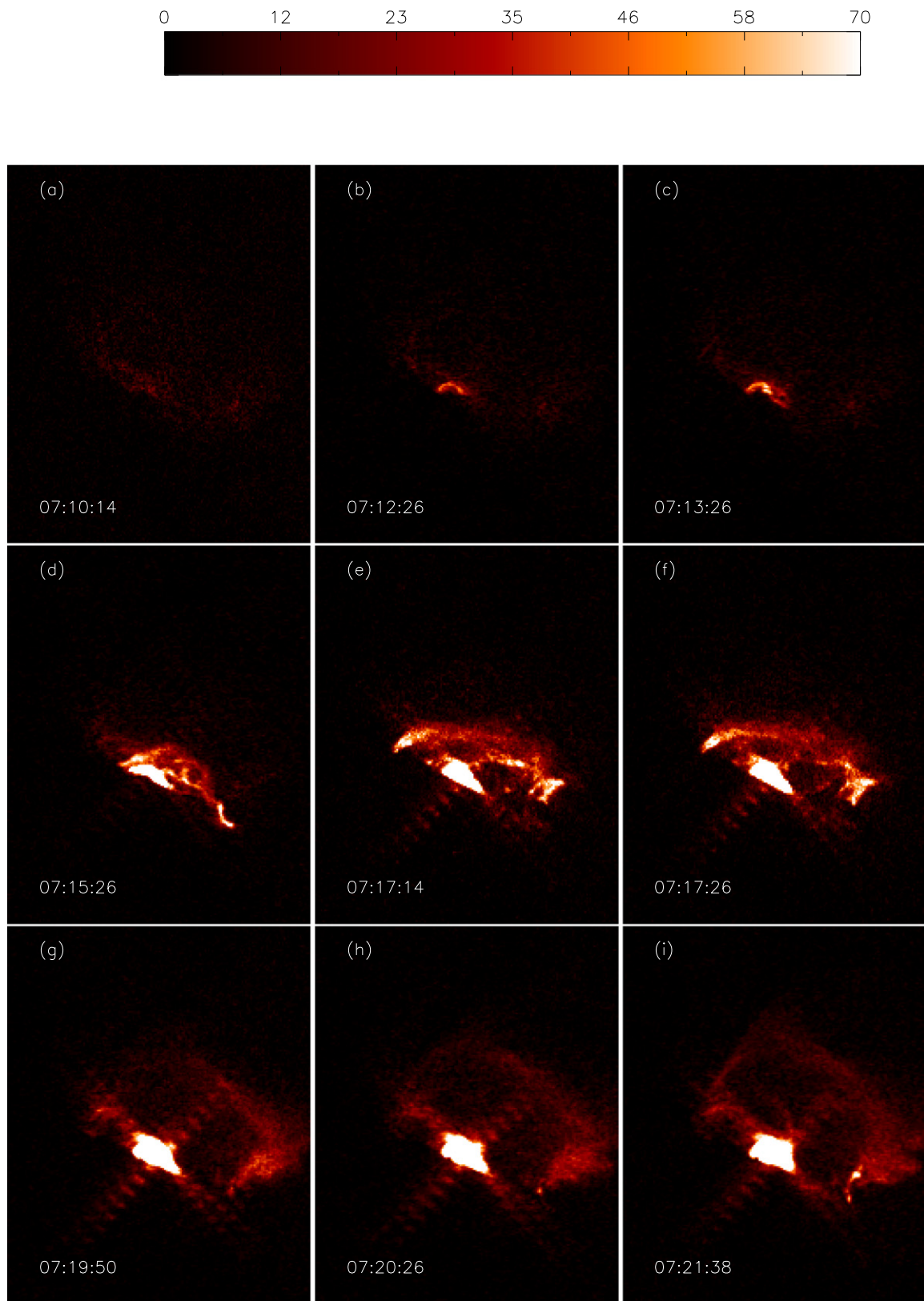


**Figure 5.** Sequence of images taken using the  $94 \text{ \AA}$  channel after the subtraction of cooler emission, showing the evolution of the flux rope structure at 7 MK (Fe xviii). The intensities are in DN/s.  
(An animation of this figure is available.)

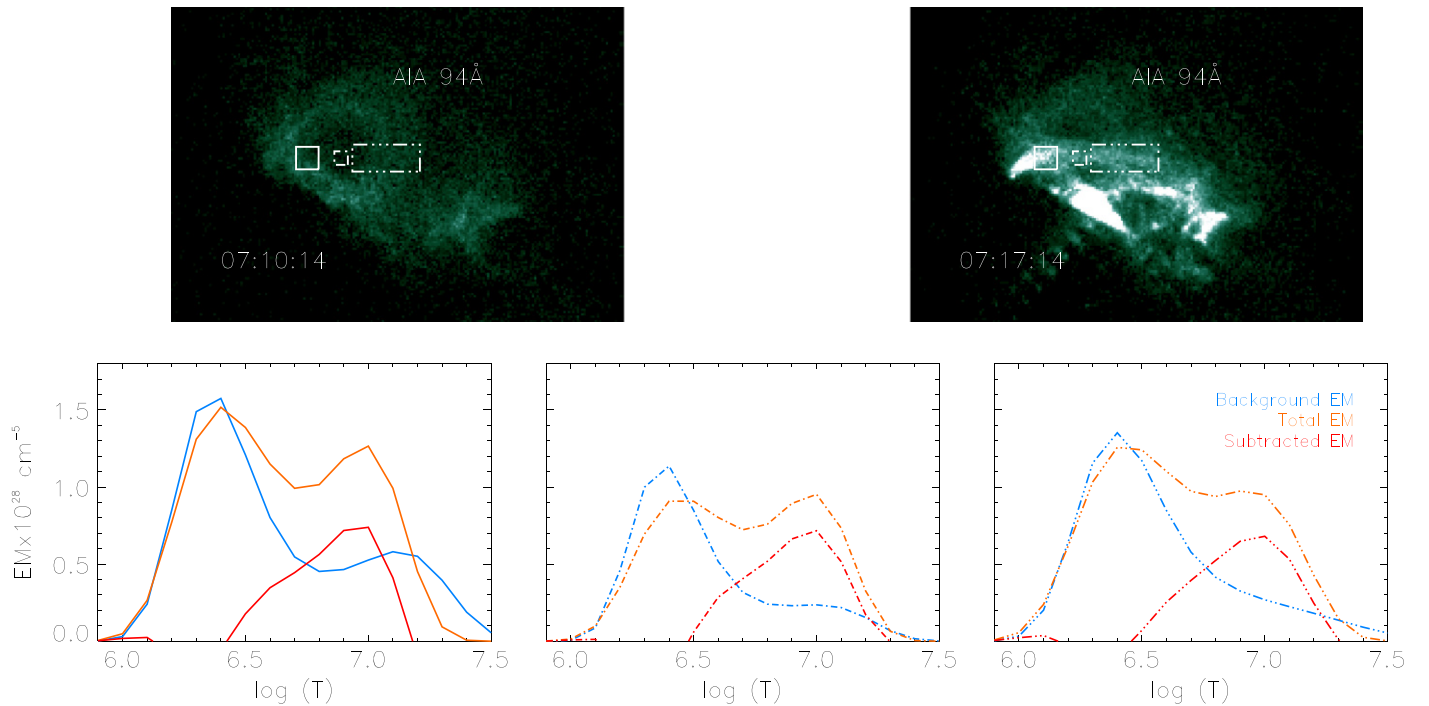


**Figure 6.** Top panel shows the regions selected to calculate the emission measure (EM) of the flux rope (right) and the background (left). The bottom panel shows the background, the total, and the subtracted emission measures of the three regions. The EM is calculated using 94, 131, 171, 193, 211, and 335 Å channels. The different linestyles in the plots correspond to the regions marked with similar linestyles in the top panel.

structure and evolution of the flux rope with time. During the initial slow-rise phase, the flux rope is visible both in the Fe XVIII and the 131 Å images, but in the later phase, the structure is visible only in Fe XVIII.

5. DEM analysis at one instant of time is performed to compare the temperature structure obtained using the algorithm and that using the DEM. The DEM analysis gives a range of temperature between  $\log T = 6.7$  and  $\log T = 7.2$  and peaks at  $\log T = 7.0$ , corresponding to the formation temperature of the Fe XVIII line at 93.9 Å.

Various previous studies have identified and analyzed flux ropes in hot as well as cool channels of AIA and provide a broad range of temperature for the flux ropes (Reeves & Golub 2011; Cheng et al. 2012; Tripathi et al. 2013; Nindos et al. 2015; Zhang et al. 2015). These studies approximately provide the temperature ranges of the features during eruptions based on observations in high-temperature channels of AIA and DEM analysis. The last two studies attribute the cause of emission in higher temperature to reconnection. Here, we provide with certainty the reconnection mechanism at the site of eruption causing the eruption and the formation of the loops.

The results obtained in this study lead us to conclude that the flux ropes are hot structures with temperatures of about 11 MK in the early phase of the eruption, which cools down to 7 MK during the evolution, very likely due to expansion. Further studies are required to make this constraint more front footing. The spontaneous formation of the flux rope is not observed, also the presence of the flux rope is not detected prior to when the eruption begins. However, the tether-cutting reconnection at the location from where the eruption begins suggests the formation of a flux rope or the creation of additional twists in an already existing flux rope due to reconnection. The isolation of the cool components of emission provides a measure to

detect the hot flux ropes. Constraints on the temperature of the flux ropes will be useful for thermodynamic modeling of flux ropes in CMEs.

We thank the referee for constructive comments that have improved the manuscript. The authors acknowledge the support from DST under the Fast Track Scheme (SERB/F/3369/2012-2013). The AIA data are courtesy of *SDO* (NASA) and the AIA consortium. CHIANTI is a collaborative project involving George Mason University, the University of Michigan (USA), and the University of Cambridge (UK). The authors thank Helen Mason for useful discussions.

## REFERENCES

- Boerner, P., Edwards, C., Lemen, J., et al. 2012, *SoPh*, **275**, 41  
 Brueckner, G. E., Howard, R. A., Koomen, M. J., et al. 1995, *SoPh*, **162**, 357  
 Cecconi, B., Bonnin, X., Hoang, S., et al. 2008, *SSRv*, **136**, 549  
 Cheng, X., Zhang, J., Saar, S. H., & Ding, M. D. 2012, *ApJ*, **761**, 62  
 Chifor, C., Mason, H. E., Tripathi, D., Isobe, H., & Asai, A. 2006, *A&A*, **458**, 965  
 Chifor, C., Tripathi, D., Mason, H. E., & Dennis, B. R. 2007, *A&A*, **472**, 967  
 Cremades, H., & Bothmer, V. 2004, *A&A*, **422**, 307  
 Del Zanna, G. 2013, *A&A*, **558**, A73  
 Del Zanna, G., Dere, K. P., Young, P. R., Landi, E., & Mason, H. E. 2015, *A&A*, **582**, A56  
 Del Zanna, G., O'Dwyer, B., & Mason, H. E. 2011, *A&A*, **535**, A46  
 Dere, K. P., Landi, E., Mason, H. E., Monsignori Fossi, B. C., & Young, P. R. 1997, *A&AS*, **125**, 149  
 Gibson, S. E., & Fan, Y. 2006, *JGRA*, **111**, 12103  
 Gibson, S. E., Fan, Y., Török, T., & Kliem, B. 2006, *SSRv*, **124**, 131  
 Gibson, S. E., Kucera, T. A., Rastawicki, D., et al. 2010, *ApJ*, **724**, 1133  
 Grevesse, N., & Sauval, A. J. 1998, *SSRv*, **85**, 161  
 Howard, R. A., Moses, J. D., Vourlidas, A., et al. 2008, *SSRv*, **136**, 67  
 Kucera, T. A., Gibson, S. E., Schmit, D. J., Landi, E., & Tripathi, D. 2012, *ApJ*, **757**, 73  
 Lemen, J. R., Akin, D. J., Boerner, P. F., et al. 2012, *SoPh*, **275**, 17



- Liu, C., Deng, N., Lee, J., et al. 2013, [ApJL](#), **778**, L36
- Mackay, D. H., Karpen, J. T., Ballester, J. L., Schmieder, B., & Aulanier, G. 2010, [SSRv](#), **151**, 333
- Martin, S. F. 1998, [SoPh](#), **182**, 107
- Moore, R. L., Sterling, A. C., Hudson, H. S., & Lemen, J. R. 2001, [ApJ](#), **552**, 833
- Nindos, A., Patsourakos, S., Vourlidas, A., & Tagikas, C. 2015, [ApJ](#), **808**, 117
- O'Dwyer, B., Del Zanna, G., Mason, H. E., Weber, M. A., & Tripathi, D. 2010, [A&A](#), **521**, A21
- Patsourakos, S., Vourlidas, A., & Stenborg, G. 2013, [ApJ](#), **764**, 125
- Reeves, K. K., & Golub, L. 2011, [ApJL](#), **727**, L52
- Schmit, D. J., Gibson, S. E., Tomczyk, S., et al. 2009, [ApJL](#), **700**, L96
- Sheeley, N. R., Jr., Warren, H. P., Lee, J., et al. 2014, [ApJ](#), **797**, 131
- Subramanian, S., Tripathi, D., Klimchuk, J. A., & Mason, H. E. 2014, [ApJ](#), **795**, 76
- Tripathi, D., Gibson, S. E., Qiu, J., et al. 2009a, [A&A](#), **498**, 295
- Tripathi, D., Isobe, H., & Mason, H. E. 2006, [A&A](#), **453**, 1111
- Tripathi, D., Kliem, B., Mason, H. E., Young, P. R., & Green, L. M. 2009b, [ApJL](#), **698**, L27
- Tripathi, D., Reeves, K. K., Gibson, S. E., Srivastava, A., & Joshi, N. C. 2013, [ApJ](#), **778**, 142
- Warren, H. P., Winebarger, A. R., & Brooks, D. H. 2012, [ApJ](#), **759**, 141
- Weber, M. A., Deluca, E. E., Golub, L., & Sette, A. L. 2004, IAU Symp. 223, Multi-Wavelength Investigations of Solar Activity, ed. A. V. Stepanov, E. E. Benevolenskaya, & A. G. Kosovichev (Cambridge: Cambridge Univ. Press), 321
- Zhang, J., Yang, S. H., & Li, T. 2015, [A&A](#), **580**, A2